





Cite this: *Chem. Commun.*, 2021,
57, 11843

Received 1st August 2021,
Accepted 13th October 2021

DOI: 10.1039/d1cc04178a

rsc.li/chemcomm

Enhanced oxygen evolution activity on mesoporous cobalt–iron oxides†

Tianmi Tang, Qiaoqiao Zhang, Xue Bai, Zhenlu Wang  and Jingqi Guan *

To solve the energy crisis and environmental pollution problems, the use of clean and renewable energy to replace fossil energy has become a top priority. The oxygen evolution reaction (OER) is the core of many renewable energy technologies. Developing low-cost and high-performance OER electrocatalysts is the key to implementing efficient energy conversion processes. Here, we synthesize ordered mesoporous iron–cobalt oxides using a hard template strategy. As a mesoporous oxide catalyst, *meso*-CoFe_{0.05}O_x exhibits low OER overpotentials of 280 and 373 mV at current densities of 10 and 100 mA cm^{−2}, respectively, and does not show deactivation for at least 18 hours at 100 mA cm^{−2}. The introduction of iron can change the electronic structure of Co, and the orbital electrons are easily transferred from cobalt to iron. The enhanced OER performance can be attributed to concerted catalysis between the iron and cobalt sites that lowers the OER energy barrier, and the large specific surface area of the porous oxide providing efficient active sites for the reaction.

With the rapid consumption of fossil fuels, we are encountering an energy crisis, environmental pollution, and climate change, which force us to develop efficient energy storage and conversion techniques.¹ The oxygen evolution reaction (OER) is a key process in these technologies, which involves a multiple-step electron transfer. A large reaction barrier will result in high overpotentials and low energy utilization.² To date, noble metal catalysts, such as iridium- and ruthenium-based materials, have been widely used as OER catalysts, but their scarcity, high cost, and poor charge–discharge stability have prevented their large-scale commercial application.^{3–5} Therefore, in recent years, more and more effort has been made to develop abundant, efficient and durable non-noble metal electrocatalysts.^{6–8}

The physical and chemical properties of transition metal oxides vary with structure. Among them, cobalt-based catalysts, such as spinel, perovskite, hydroxyl oxides, and layered hydroxides

have been vigorously studied as OER electrocatalysts. Spinel type cobalt-based metal oxides have attracted much attention because of their multifunctional properties.⁹ The spinel Co₃O₄ contains one Co(II) ion in the tetrahedron (Co²⁺–Td) and two Co(III) ions in the octahedron (Co³⁺–Oh), and exhibits excellent OER properties.¹⁰ Although the Co⁴⁺ ion is the active site for the OER, the adjacent Co³⁺–Oh can also promote OER kinetics.¹¹ Nevertheless, only the adjacent surface Co₃O₄ can be oxidized to amorphous CoO_x(OH)_y with a change from Co²⁺–Td to Co³⁺–Oh.

SBA-15 with *P6mm* symmetry is a mesoporous silica molecular sieve, which can be used as a hard template to prepare porous metal oxides. Metal oxides were usually prepared by wet leaching with the assistance of hard templates.¹² During the calcination process, a slow heating rate is adopted to allow the molten metal precursors to fully spread into the silica pores and then decompose into the homologous metal oxides. After removing the SBA-15 template, the obtained mesoporous oxides usually have a large specific surface area.¹³ Calcination temperature, silica pore size and precursor loading capacity will determine the order degree and particle size of the mesoporous structure. The introduction of iron into cobalt oxides can fine-tune the electronic structure to facilitate the adsorption of reactants. For instance, Chen *et al.* reported that iron ions at octahedral sites interacting with cobalt at tetrahedral sites in spinel structures promoted the OER.¹⁴ Wang *et al.* synthesized iron-doped α -Co(OH)₂, and found that the modified redox characteristics made the OER more effective.¹⁵ In this work, a new type of mesoporous Co–Fe oxide (*meso*-CoFe_{*n*}O_{*x*}, *n* represents the molar ratio of Fe/Co atoms) was synthesized by using SBA-15 as the hard template, which shows high OER activity and excellent stability under alkaline conditions.

The structure of the as-synthesized *meso*-CoFeO_{*x*} was analyzed using XRD. As shown in Fig. 1a, the diffraction angle of *meso*-CoFe_{0.05}O_{*x*} accurately matches the crystal planes of spinel Co₃O₄ (JCPDS No. 76-1802), indicating that the Fe ions are highly dispersed in Co₃O₄ and do not destroy the structure.¹⁶ From the FT-IR spectra (Fig. 2b), the vibration peaks of the Si–O–Si bond in the SBA-15 are centered at *ca.* 1086, 969, 801, and 461 cm^{−1}, which

Institute of Physical Chemistry, College of Chemistry, Jilin University,
2519 Jiefang Road, Changchun 130021, P. R. China. E-mail: guanjq@jlu.edu.cn

† Electronic supplementary information (ESI) available. See DOI: 10.1039/d1cc04178a

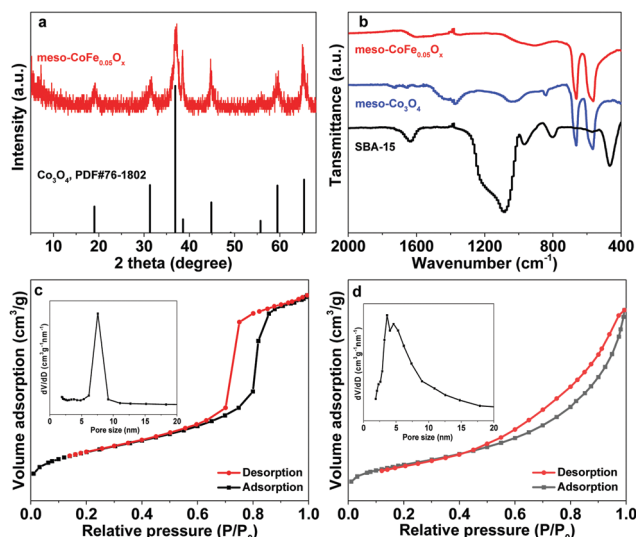


Fig. 1 (a) XRD patterns of SBA-15 and *meso*-CoFe_{0.05}O_x. (b) FT-IR spectra of *meso*-CoFe_{0.05}O_x, *meso*-Co₃O₄ and SBA-15. (c and d) N₂ adsorption-desorption isotherms and pore size distributions of (c) SBA-15 and (d) *meso*-CoFe_{0.05}O_x.

are absent for *meso*-CoFe_{0.05}O_x, which confirms that the template SBA-15 was removed after alkaline treatment. Moreover, there are two new strong vibration peaks at *ca.* 661 and 562 cm⁻¹ in *meso*-CoFe_{0.05}O_x, which are slightly different from those of the Co-O

bond at 664 and 567 cm⁻¹ due to the influence of Fe-doping.¹⁷ From the Raman patterns, the five peaks of *meso*-CoFe_{0.05}O_x are obviously deflected from those of *meso*-Co₃O₄ (Fig. S1, ESI†), which suggests that the Fe ions were successfully immobilized into the lattice of Co₃O₄.¹⁸ Fig. 2c and d show the N₂ adsorption-desorption isotherms and pore size distribution of SBA-15 and *meso*-CoFe_{0.05}O_x, both of which exhibit typical IV isotherms, which indicates the presence of a mesoporous structure in the synthesized *meso*-CoFe_{0.05}O_x.¹⁹ The BET specific surface area of *meso*-CoFe_{0.05}O_x is 76.6 m² g⁻¹, which is lower than that of SBA-15 (553.5 m² g⁻¹). The pore size of *meso*-CoFe_{0.05}O_x is mainly centred at around 3.6 and 4.6 nm, and is smaller than that (7.5 nm) of SBA-15.

The morphology of *meso*-CoFe_{0.05}O_x was disclosed using SEM and TEM. As displayed in Fig. 2a, a cellular structure can be observed, indicating that *meso*-CoFe_{0.05}O_x possesses mesopores. From Fig. 2b, the mesopores in *meso*-CoFe_{0.05}O_x are clearly observable. The elemental composition and distribution of *meso*-CoFe_{0.05}O_x was measured using SEM-EDS, and shows that Fe, Co and O are evenly distributed in the selected area and that the Fe ions were successfully doped into the framework of cobalt oxide. The element analysis revealed that the Co/Fe ratio of *meso*-CoFe_{0.05}O_x is very close to 1 : 0.05. From the HRTEM results, the crystal plane spacing of *meso*-CoFe_{0.05}O_x is *ca.* 0.253 nm, which is different from that of cobalt oxide, and further testifies that iron ions were doped into the lattice of cobalt oxide (Fig. S2, ESI†).

The elemental compositions and metal valences of *meso*-CoFe_{0.05}O_x were studied using XPS. As demonstrated in Fig. 3, the measured spectrum shows the presence of the elements Fe, Co and O in *meso*-CoFe_{0.05}O_x. The high resolution Fe 2p_{3/2} peak can be deconvoluted into two peaks at binding energies of 710.9 eV and 713.1 eV, and indicates that Fe exists as Fe²⁺ and Fe³⁺ (Fig. 3b).^{20,21} In the Co 2p spectrum, the peak of Co 2p_{3/2} and Co 2p_{1/2} is located at 779.7 eV and 794.8 eV, respectively.

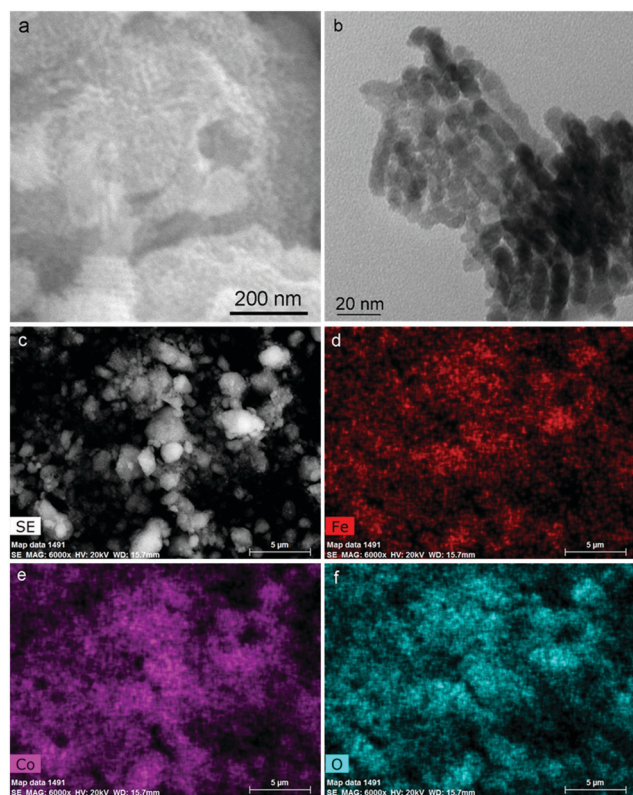


Fig. 2 (a) SEM image and (b) TEM image of *meso*-CoFe_{0.05}O_x. (c) SEM image used in the EDS mapping, and (d–f) the corresponding EDS mapping of the elements Fe, Co, and O.

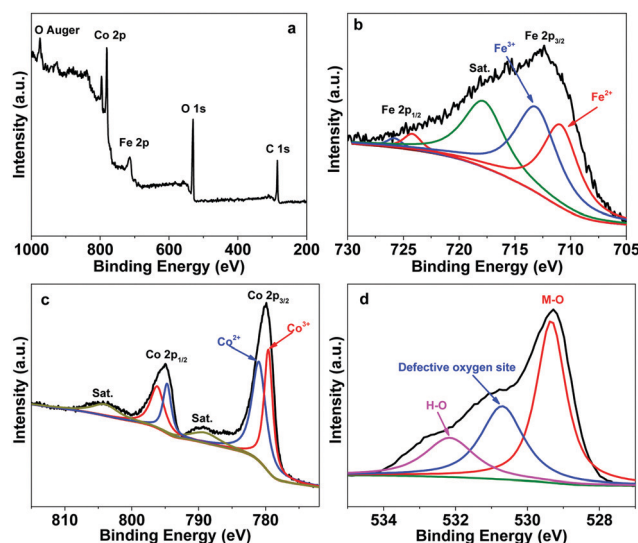


Fig. 3 (a) XPS survey spectrum, and (b–d) high-resolution XPS spectra of Fe 2p (b), Co 2p (c), and O 1s (d) of *meso*-CoFe_{0.05}O_x.

The high resolution Co 2p_{3/2} peak can be deconvoluted into two peaks at 779.6 and 781.0 eV, which correspond to Co³⁺ and Co²⁺, respectively (Fig. 3c).^{22,23} The O 1s peak can be fitted into three peaks at 529.3, 530.7 and 532.2 eV, which are due to M–O (M = Fe and Co), defective oxygen sites and surface hydroxyl groups, respectively (Fig. 3d).^{24,25}

The OER performance of the as-prepared mesoporous cobalt–iron oxides was assessed using LSV measurements in 1.0 M KOH. As exhibited in Fig. 4a, commercial Co₃O₄ needs a high overpotential (η_{10}) of 386 mV to reach a current density of 10 mA cm^{−2}. The OER activity can be improved by transforming the bulk Co₃O₄ to mesoporous Co₃O₄, and *meso*-Co₃O₄ exhibits an overpotential (η_{10}) of 359 mV. The OER activity can be immensely enhanced by introducing a small amount of Fe ions. For example, *meso*-CoFe_{0.01}O_x exhibits an η_{10} of 340 mV (Fig. S3, ESI†). With an increasing Fe content, the OER activity increases and reaches a maximum at an Fe/Co ratio of 0.05. *meso*-CoFe_{0.05}O_x requires an overpotential of only 280 and 373 mV to achieve current densities of 10 and 100 mA cm^{−2}, respectively, which surpasses or is comparable to most Fe/Co-based electrocatalysts reported previously (Table S1, ESI†). A further increase of the Fe content would lead to a decrease in electrocatalytic activity. For instance, *meso*-CoFe_{0.075}O_x and *meso*-CoFe_{0.1}O_x require an η_{10} of 321 and 377 mV, respectively. The excellent OER activity is further reflected by its small Tafel slope value (68 mV dec^{−1}) (Fig. 4b), which indicates an OER rate-determining step following the first electron transfer.²⁶ The doping of iron modifies the electronic property of Co, and thus influences the redox ability (Fig. S4, ESI†).^{15,27} The introduction of iron can change the electronic state of Co, and the orbital electrons are easily transferred from cobalt to iron.²⁸ Moreover, the valence state and e_g electrons of Co³⁺ can be adjusted by introducing high spin state Fe³⁺ into the octahedral position since Fe³⁺ tends to occupy the octahedral site due to its low formation energy. The formation of Fe³⁺–O will reduce the lattice symmetry and split the d orbital of Co³⁺.²⁹ The interaction between them leads to excellent OER catalytic activity.²⁸

The electrochemical surface area (ECSA) can be used to reveal the available electrocatalytically active sites for the OER, which can be measured by comparing the capacitance of the double layer (C_{dl}).³⁰ As illustrated in Fig. S5–S7 (ESI†), the ECSA of *meso*-CoFe_{0.05}O_x is 32 m² g^{−1}, and is larger than those of commercial Co₃O₄ (6 m² g^{−1}) and *meso*-Co₃O₄ (10 m² g^{−1}), which implies that more active sites are accessible in *meso*-CoFe_{0.05}O_x. The ECSA of *meso*-CoFe_{0.05}O_x is also larger than those of *meso*-CoFe_{0.01}O_x (17 m² g^{−1}), *meso*-CoFe_{0.025}O_x (19 m² g^{−1}), *meso*-CoFe_{0.075}O_x (25 m² g^{−1}) and *meso*-CoFe_{0.1}O_x (21 m² g^{−1}) (Fig. S8–S11, ESI†).

Electrochemical impedance spectroscopy (EIS) was used to investigate the resistance involved in the system and the dynamics for OER (Fig. S12, ESI†). The charge transfer resistance (R_{ct}) of *meso*-CoFe_{0.05}O_x is ca. 6.8 Ω cm², which is far smaller than those of *meso*-Co₃O₄ and commercial Co₃O₄, and illustrates the advantageous OER kinetics of *meso*-CoFe_{0.05}O_x. The OER energy barrier (ΔG) on *meso*-CoFe_{0.05}O_x is calculated to be ca. 261 kJ mol^{−1} according to eqn (1–4), which is far lower than those on commercial Co₃O₄ (385 kJ mol^{−1}) and *meso*-Co₃O₄ (332 kJ mol^{−1}), which indicates that the introduction of a small amount of Fe into the Co-based oxide system can significantly lower the OER energy barrier due to concerted catalysis between the Fe and Co sites.

$$j = j_0 \times e^{\frac{(1-\alpha)F(E-E_0)}{RT}} \quad (1)$$

$$k = Ae^{\frac{-\Delta G}{RT}} \quad (2)$$

$$\Delta G = \Delta G_0 - (1 - \alpha)nFE \quad (3)$$

$$\alpha = 1 - \frac{1}{1 - \frac{\alpha_1}{\alpha_2}} \quad (4)$$

Where J is the exchange current density, the Faraday constant (F) is 96485 C mol^{−1}, the universal gas constant (R) is 8.314 J mol^{−1}, T is the experimental temperature, the number of electrons transferred (n) in the OER reaction is 4, α is the Tafel slope, and k is the reaction rate constant.

The stability of *meso*-CoFe_{0.05}O_x was evaluated by loading it onto a graphite sheet (Fig. 4c and d). *meso*-Fe_{0.05}CoO_x exhibits excellent durability at different current densities (Fig. 4c). At a high current density of 100 mA cm^{−2}, *meso*-Fe_{0.05}CoO_x does not show any deactivation after continuous operation for 18 hours (Fig. 4d). The OER polarization curve of *meso*-CoFe_{0.05}O_x after the stability test is similar to the initial one, which indicates excellent OER stability (Fig. S13, ESI†). The long-term stability of *meso*-CoFe_{0.05}O_x can be attributed to the spinel phase, which has a variety of oxidation states and can provide faster ion transport and charge transfer.³¹ The introduction of iron caused the d band centre of Co to move down, and further increased the OER tolerance of *meso*-CoFe_{0.05}O_x.³² The mesoporous structure favours exposure of the catalytic active centre to the electrolyte and promotes the release of oxygen, which reduces the mass transfer resistance and thus improves the OER activity. The electron interaction between iron and cobalt can provide more active sites and promote water oxidation.⁸

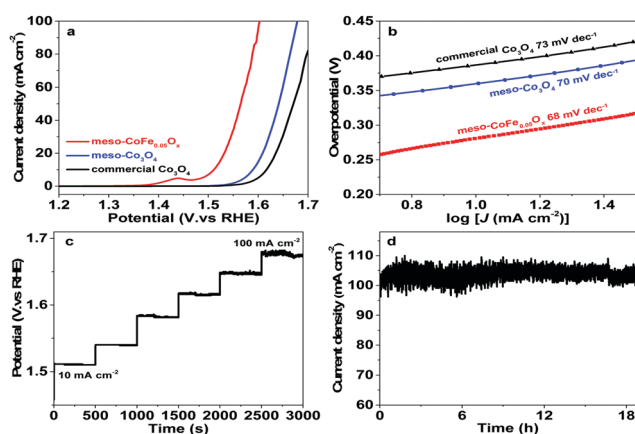


Fig. 4 (a) OER polarization curves. (b) Tafel plots. (c) Multi-current electrochemical process of *meso*-CoFe_{0.05}O_x. (d) Chronoamperometric measurements.

From the SEM and TEM images and the XRD pattern of *meso*-CoFe_{0.05}O_x after OER, the morphology and structure do not change significantly, which further confirms the excellent stability (Fig. S14 and S15, ESI†).

The chemical compositions and metal valences in *meso*-CoFe_{0.05}O_x after OER electrocatalysis were studied using XPS. From Fig. S16 (ESI†), it can be seen that the relative amount of Fe³⁺/Fe²⁺ on the *meso*-CoFe_{0.05}O_x surface increases from 1.1 : 1 to 1.8 : 1 after OER electrocatalysis, and confirms that Fe²⁺ was partially oxidized to Fe³⁺.³³ Meanwhile, some of the Co²⁺ was also oxidized to the higher valence Co³⁺ during the OER.³⁴ Furthermore, the defective oxygen sites also increased during OER electrocatalysis, which indicates that surface and/or lattice oxygen species participated in the reaction.

To sum up, we have successfully synthesized mesoporous cobalt-iron oxides using a hard template strategy. *meso*-CoFe_{0.05}O_x exhibited high OER activity (η_{10} = 280 mV, and η_{100} = 373 mV) and outstanding stability at 100 mA cm⁻² in alkaline aqueous solutions. Compared with commercial Co₃O₄ and *meso*-Co₃O₄, *meso*-CoFe_{0.05}O_x showed a lower OER energy barrier due to its large specific surface area, small charge transfer resistance, and concerted catalysis of the Fe and Co sites. This study offers a facile strategy for the synthesis of mesoporous mixed oxide electrocatalysts for energy conversion and storage devices.

This work was supported by the National Natural Science Foundation of China (22075099), and the Natural Science Foundation of Jilin Province (20180101291JC).

Conflicts of interest

There are no conflicts to declare.

Notes and references

- 1 P. G. Bruce, S. A. Freunberger, L. J. Hardwick and J.-M. Tarascon, *Nat. Mater.*, 2011, **11**, 19–29.
- 2 H. Dau, C. Limberg, T. Reier, M. Risch, S. Roggan and P. Strasser, *ChemCatChem*, 2010, **2**, 724–761.
- 3 N.-T. Suen, S.-F. Hung, Q. Quan, N. Zhang, Y.-J. Xu and H. M. Chen, *Chem. Soc. Rev.*, 2017, **46**, 337–365.
- 4 J. Bai, S.-H. Han, R.-L. Peng, J.-H. Zeng, J.-X. Jiang and Y. Chen, *ACS Appl. Mater. Interfaces*, 2017, **9**, 17195–17200.
- 5 Y. Zhao, J. Bai, X.-R. Wu, P. Chen, P.-J. Jin, H.-C. Yao and Y. Chen, *J. Mater. Chem. A*, 2019, **7**, 16437–16446.
- 6 X. Wang, A. Dong, Y. Hu, J. Qian and S. Huang, *Chem. Commun.*, 2020, **56**, 10809–10823.
- 7 X. Wang, L. Chai, J. Ding, L. Zhong, Y. Du, T.-T. Li, Y. Hu, J. Qian and S. Huang, *Nano Energy*, 2019, **62**, 745–753.
- 8 J. Ding, Q. Sun, L. Zhong, X. Wang, L. Chai, Q. Li, T.-T. Li, Y. Hu, J. Qian and S. Huang, *Electrochim. Acta*, 2020, **354**, 136716.
- 9 M.-S. Park, J. Kim, K. J. Kim, J.-W. Lee, J. H. Kim and Y. Yamauchi, *Phys. Chem. Chem. Phys.*, 2015, **17**, 30963–30977.
- 10 S. Sun, Y. Sun, Y. Zhou, S. Xi, X. Ren, B. Huang, H. Liao, L. P. Wang, Y. Du and Z. J. Xu, *Angew. Chem., Int. Ed.*, 2019, **58**, 6042–6047.
- 11 M. Zhang, M. de Respinis and H. Frei, *Nat. Chem.*, 2014, **6**, 362–367.
- 12 F. Kleitz, S. Hei Choi and R. Ryoo, *Chem. Commun.*, 2003, 2136–2137.
- 13 A. Yunesnialehi, H. Shagholani, A. Nikpay, M. Ghorbani, M. Soleimani lashkenari and M. Soltani, *Int. J. Pharm.*, 2019, **555**, 28–35.
- 14 S.-F. Hung, Y.-Y. Hsu, C.-J. Chang, C.-S. Hsu, N.-T. Suen, T.-S. Chan and H. M. Chen, *Adv. Energy Mater.*, 2018, **8**, 1701686.
- 15 H. Jin, S. Mao, G. Zhan, F. Xu, X. Bao and Y. Wang, *J. Mater. Chem. A*, 2017, **5**, 1078–1084.
- 16 Q. Zhang, X. Fu, Q. Kan and J. Guan, *Ind. Eng. Chem. Res.*, 2019, **58**, 4774–4779.
- 17 S. Xiong, S. Weng, Y. Tang, L. Qian, Y. Xu, X. Li, H. Lin, Y. Xu, Y. Jiao and J. Chen, *J. Colloid Interface Sci.*, 2021, **602**, 355–366.
- 18 J. Zhang, S. Cui, Y. Ding, X. Yang, K. Guo and J. Zhao, *Ceram. Int.*, 2018, **44**, 7858–7866.
- 19 X.-J. Ma, Y.-J. Yu, J.-L. Xing, T.-Q. Yang, K. F. Lam, Q.-S. Xue, B. Albel, L. Bonnevot and K. Zhang, *Microporous Mesoporous Mater.*, 2014, **200**, 182–189.
- 20 P. S. Bagus, C. J. Nelin, C. R. Brundle, B. V. Crist, N. Lahiri and K. M. Rosso, *J. Chem. Phys.*, 2021, **154**, 094709.
- 21 T. H. Chiang, S.-C. Sun and Y.-S. Chen, *J. Taiwan Inst. Chem. Eng.*, 2020, **115**, 175–186.
- 22 N. Koteeswara Reddy, S. Winkler, N. Koch and N. Pinna, *ACS Appl. Mater. Interfaces*, 2016, **8**, 3226–3232.
- 23 S. Wan, J. Qi, W. Zhang, W. Wang, S. Zhang, K. Liu, H. Zheng, J. Sun, S. Wang and R. Cao, *Adv. Mater.*, 2017, **29**, 1700286.
- 24 N. Liu and J. Guan, *Mater. Today Energy*, 2021, **21**, 100715.
- 25 S. Zhang, N. Wei, Z. Yao, X. Zhao, M. Du and Q. Zhou, *Int. J. Hydrogen Energy*, 2021, **46**, 5286–5295.
- 26 M. S. Burke, M. G. Kast, L. Trotochaud, A. M. Smith and S. W. Boettcher, *J. Am. Chem. Soc.*, 2015, **137**, 3638–3648.
- 27 K. Malaie and M. R. Ganjali, *Mater. Chem. Phys.*, 2020, **253**, 123339.
- 28 K. Ge, S. Sun, Y. Zhao, K. Yang, S. Wang, Z. Zhang, J. Cao, Y. Yang, Y. Zhang, M. Pan and L. Zhu, *Angew. Chem., Int. Ed.*, 2021, **60**, 12097–12102.
- 29 X. Gao, J. Liu, Y. Sun, X. Wang, Z. Geng, F. Shi, X. Wang, W. Zhang, S. Feng, Y. Wang and K. Huang, *Inorg. Chem. Front.*, 2019, **6**, 3295–3301.
- 30 H. Fei, J. Dong, M. J. Arellano-Jiménez, G. Ye, N. Dong Kim, E. L. G. Samuel, Z. Peng, Z. Zhu, F. Qin, J. Bao, M. J. Yacaman, P. M. Ajayan, D. Chen and J. M. Tour, *Nat. Commun.*, 2015, **6**, 8668.
- 31 S. Natarajan, S. Anantharaj, R. J. Tayade, H. C. Bajaj and S. Kundu, *Dalton Trans.*, 2017, **46**, 14382–14392.
- 32 J. Shan, C. Ye, S. Chen, T. Sun, Y. Jiao, L. Liu, C. Zhu, L. Song, Y. Han, M. Jaroniec, Y. Zhu, Y. Zheng and S.-Z. Qiao, *J. Am. Chem. Soc.*, 2021, **143**, 5201–5211.
- 33 L. An, J. Feng, Y. Zhang, Y.-Q. Zhao, R. Si, G.-C. Wang, F. Cheng, P. Xi and S. Sun, *Nano Energy*, 2019, **57**, 644–652.
- 34 Q. Du, P. Su, Z. Cao, J. Yang, C. A. H. Price and J. Liu, *Sustainable Mater. Technol.*, 2021, **29**, e00293.